

# Unlocking the Optoelectronic Potential of $\text{AGeX}_3$ ( $\text{A} = \text{Ca}, \text{Sr}, \text{Ba}$ ; $\text{X} = \text{S}, \text{Se}$ ): A Sustainable Alternative in Chalcogenide Perovskites

Ayan Chakravorty, Surajit Adhikari\*, and Priya Johari\*

*Department of Physics, School of Natural Sciences,  
Shiv Nadar Institution of Eminence, Greater Noida,  
Gautam Buddha Nagar, Uttar Pradesh 201314, India.*

The quest for environmentally benign and stable optoelectronic materials has intensified, and chalcogenide perovskites (CPs) have emerged as promising candidates owing to their non-toxic composition, stability, small bandgaps, large absorption coefficients. However, a detailed theoretical study of excitonic and polaronic properties of these materials remains underexplored due to high computational demands. Herein, we present a comprehensive theoretical investigation of Germanium-based CPs,  $\text{AGeX}_3$  ( $\text{A} = \text{Ca}, \text{Sr}, \text{Ba}$ ;  $\text{X} = \text{S}, \text{Se}$ ), which adopt distorted perovskite structures ( $\beta$ -phase) with an orthorhombic crystal structure (space group :  $Pnma$ ) by utilizing state-of-the-art density functional theory (DFT), density functional perturbation theory (DFPT), and many-body perturbation theory (GW and Bethe-Salpeter equation). Our calculations reveal that these materials are thermodynamically and mechanically stable, with the bandgaps calculated using  $G_0W_0@PBE$  ranging from 0.646 to 2.001 eV – suitable for optoelectronic devices. We analyze the ionic and electronic contributions to dielectric screening using DFPT and BSE methods, finding that the electronic component dominates. The exciton binding energies range from 0.03 to 73.63 meV, indicating efficient exciton dissociation under ambient conditions. Additionally, these perovskites exhibit low to high polaronic mobilities ( $1.67\text{--}167.65\text{ cm}^2\text{V}^{-1}\text{s}^{-1}$ ), exceeding many lead-free CPs and halide perovskites due to reduced carrier-phonon interactions. The unique combination of wide tunable bandgaps, low exciton binding energies, and enhanced charge-carrier mobility highlights  $\text{AGeX}_3$  as a potential material for next-generation optoelectronic applications. These compounds are stable, high-performing, and eco-friendly, showing great promise for experimental realization and device integration.

## I. INTRODUCTION:

Inorganic-organic hybrid perovskites (IOHPs) have emerged as exceptional contenders, achieving a remarkable surge in power conversion efficiency (PCE) upto 26.7% within a decade with their exceptional optoelectronic properties such as tunable bandgaps, strong light absorption, long carrier diffusion lengths, and remarkable defect tolerance which make them highly attractive for next-generation devices [1, 2]. However, large-scale commercialization remains hindered by critical drawbacks, including lead toxicity and intrinsic instability arising from volatile organic cations [3, 4]. These drawbacks have spurred the search for alternative perovskite materials that retain the superior optoelectronic properties of IOHPs while addressing their limitations. In contrast, chalcogenide perovskites (CPs) are gaining prominence as promising alternatives, offering superior stability, earth-abundant constituents, and a non-toxic composition [5–8]. CPs exhibit several advantageous properties, such as optimal bandgaps, high optical absorption coefficients, desirable charge carrier mobility, and excellent power conversion efficiency (PCE), which collectively enhance their suitability for optoelectronic applications [8–12]. The successful synthesis of CPs, further underscores their viability as next-generation semiconductors [6]. These attributes firmly establish CPs as frontrunners in the pursuit of high-performance, eco-friendly, lead-free optoelectronic materials.

Similar to halide perovskites, CPs adopt the general chemical formula  $\text{ABX}_3$  [13], where “A” represents divalent alkaline-earth metals ( $\text{Ca}^{2+}$ ,  $\text{Sr}^{2+}$ ,  $\text{Ba}^{2+}$ ), “B” is a tetravalent metal cations ( $\text{Ti}^{4+}$ ,  $\text{Zr}^{4+}$ ,  $\text{Hf}^{4+}$ ,  $\text{Sn}^{4+}$ ,  $\text{Ge}^{4+}$ ), and “X” is a chalcogen anion ( $\text{S}^{2-}$ ,  $\text{Se}^{2-}$ ). CPs primarily crystallize in two orthorhombic phases at room temperature: the needle-like  $\text{NH}_4\text{CdCl}_3$ -type and the distorted  $\text{GdFeO}_3$ -type, both sharing same space group  $Pnma$  (No. 62) [12, 13]. Experimentally, the distorted phase of  $\text{CaZrS}_3$ ,  $\text{SrZrS}_3$ ,  $\text{BaZrS}_3$ ,  $\text{CaHfS}_3$ ,  $\text{SrHfS}_3$ , and  $\text{BaHfS}_3$  as well as the needle-like phase of  $\text{SrZrS}_3$ ,  $\text{SrZrSe}_3$ , and  $\text{SrHfSe}_3$  have been synthesized [13–16]. Perera et al. achieved  $\text{AZrS}_3$  ( $\text{A} = \text{Ca}, \text{Sr}, \text{Ba}$ ) synthesis via high-temperature sulfurization [17], while recent studies reported  $\text{CaSnS}_3$  synthesis [18]. The phase stability of CPs was theoretically predicted by Sun et al., and first-principles calculations have highlighted their promising optoelectronic properties [12].

Several studies have primarily focused on Zr- and Hf-based CPs, which exhibit exciton binding energies ranging from 0.02 to 0.26 eV [9, 10, 19], comparable to or slightly higher than those of conventional HPs (0.01–0.10 eV)

\* ac900@snu.edu.in, sa731@snu.edu.in, priya.johari@snu.edu.in

[20, 21]. However, these materials suffer from reduced charge carrier mobility ( $6.84\text{--}77.59\text{ cm}^2\text{V}^{-1}\text{s}^{-1}$ ) and lower optoelectronic performance compared to conventional HPs. These limitations arise due to prominent polaronic effects that hinder charge transport, reducing their effectiveness for optoelectronic applications. These challenges have steered researchers toward Ge- and Sn-based systems, which exhibit improved charge transport and optoelectronic properties. Recent first-principles calculations highlight the potential of Sn and Ge as a B-site cation, with distorted  $\text{SrSnX}_3$  ( $X = \text{S, Se}$ ) perovskites emerging as promising materials based on their optoelectronic properties [22–24]. Experimental investigations have further substantiated this potential through the successful synthesis of distorted  $\text{CaSnS}_3$  perovskite at  $500^\circ\text{C}$  [25]. Notably, needle-like CPs like  $\text{BaSnS}_3$  and  $\text{SrSnS}_3$  exhibit higher bandgaps ( $1.91\text{--}2.04\text{ eV}$ ) and lower theoretical efficiency ( $21.80\%$ ) [10], whereas distorted  $\text{CaSnS}_3$  addresses these limitations with an optimal bandgap of  $1.43\text{ eV}$  and a significantly higher theoretical efficiency of up to  $32.45\%$  [10], emphasizing the superior optoelectronic performance of distorted phases.

Motivated by these findings, we extend our focus to Ge-based CPs as the next step in CP research. As a group-IV element alongside Sn, Ge shares similar valence and structural compatibility. Additionally, Ge has been widely recognized as a promising material for optoelectronics due to its proven transport properties, which have been extensively demonstrated in high-performance electronic applications [26]. Moreover, materials explored for superior optoelectronic performance are significantly influenced by exciton formation, as efficient charge transport relies on the thermal dissociation of excitons into free carriers, while polaronic effects, governed by electron-phonon interactions, dictate charge carrier dynamics and transport mechanisms. The multiple photophysical phenomena in these materials can be understood through electron-phonon interactions and polaron transport [27, 28]. Despite the potential impact of these effects, a detailed theoretical investigation of their role in Ge-based CPs remain largely unexplored, presenting a significant research gap. To address this, we conduct a comprehensive first-principles investigation of Ge-based CPs to evaluate their optoelectronic properties and assess their viability for next-generation optoelectronic applications.

Building on the promising potential of Ge-based CPs as highlighted in the preceding discussions, we have undertaken a thorough exploration of their electronic, optical, excitonic, and polaronic properties of the distorted phase of  $\text{AGeX}_3$  ( $A = \text{Ca, Sr, Ba}$ ;  $X = \text{S, Se}$ ) using a combination of density functional theory (DFT) [29, 30], density functional perturbation theory (DFPT) [31], and many-body perturbation theory techniques like GW and Bethe-Salpeter Equation (BSE) [32, 33]. The crystal structures are optimized with the PBE exchange-correlation functional [34], and their electronic properties are computed using the PBE xc-functional [34], hybrid HSE06 functional [35] and  $G_0W_0@PBE$  [36, 37] methodology. Our calculations reveal that  $\text{AGeX}_3$  CPs exhibit bandgaps in the optimal range for optoelectronics ( $0.646\text{--}2.001\text{ eV}$ ), alongside exciton binding energies ( $0.03\text{--}73.63\text{ meV}$ ) and polaronic mobilities (upto  $167.65\text{ cm}^2\text{V}^{-1}\text{s}^{-1}$ ) that rival or surpass conventional halide perovskites [20, 38, 39]. Utilizing the DFPT technique, we compute the ionic contributions to the dielectric function and evaluate polaronic properties using the Fröhlich model [40]. Finally, some  $\text{AGeX}_3$  compounds exhibit very high polaron mobility, all possess low exciton binding energies, and feature low effective masses, indicating excellent charge carrier mobility which underscore the immense potential of Ge-based CPs as sustainable, lead-free candidates for next-generation optoelectronic and photovoltaic technologies.

## II. COMPUTATIONAL DETAILS:

In this study, first-principles density functional theory (DFT) [29, 30] and many-body perturbation theory (MBPT) [32, 33] calculations were performed using the Vienna Ab initio Simulation Package (VASP) [41, 42]. The interactions between valence electrons and atomic cores were modeled using the projected augmented wave (PAW) method [43], with the following valence electron configurations for the pseudopotentials: Ca ( $3s^2 3p^6 4s^2$ ), Sr ( $4s^2 4p^6 5s^2$ ), Ba ( $5s^2 5p^6 6s^2$ ), Ge ( $3d^{10} 4s^2 4p^2$ ), S ( $3s^2 3p^4$ ), and Se ( $4s^2 4p^4$ ). The exchange-correlation (xc) interactions were treated using the Perdew-Burke-Ernzerhof (PBE) functional within the generalized gradient approximation (GGA) [34]. Structural optimization was performed by minimizing the total energy with the conjugate gradient method to obtain equilibrium structural parameters. A plane-wave cutoff energy of  $400\text{ eV}$  was used, and convergence criteria for self-consistent field iterations and geometry relaxations were set to  $10^{-6}\text{ eV}$  for energy and  $0.01\text{ eV}/\text{\AA}$  for Hellmann-Feynman forces on each atom. The  $\Gamma$ -centered k-point grid of  $8 \times 8 \times 6$  was employed for structural optimization. PBE functionals are known to underestimate band gaps and optical properties due to self-interaction errors. To achieve more accurate electronic structures, hybrid Heyd-Scuseria-Ernzerhof (HSE06) [35] and many-body perturbation theory ( $G_0W_0@PBE$ ) [36, 37] calculations were performed. The band structures, including spin-orbit coupling effects, were computed with the PBE functional. Additionally, the density of states (DOS) was calculated using the HSE06 hybrid functional. We performed Bethe-Salpeter equation (BSE) calculations on top of single-shot  $G_0W_0@PBE$  to accurately determine the optical properties which explicitly accounts the electron-hole interactions [44, 45]. The BSE calculations employed a  $\Gamma$ -centered  $3 \times 3 \times 2$  k-grid and 640 bands to ensure convergence. The electron-hole kernel was constructed using 24 occupied and 24 unoccupied states. Furthermore, ionic contributions to the dielectric

function were computed using density functional perturbation theory (DFPT) [31] with an  $8 \times 8 \times 6$  k-point grid. Post-processing of elastic, electronic, and optical properties was conducted using the VASPKIT package [46].

### III. RESULTS AND DISCUSSIONS:

#### A. Structural Properties:

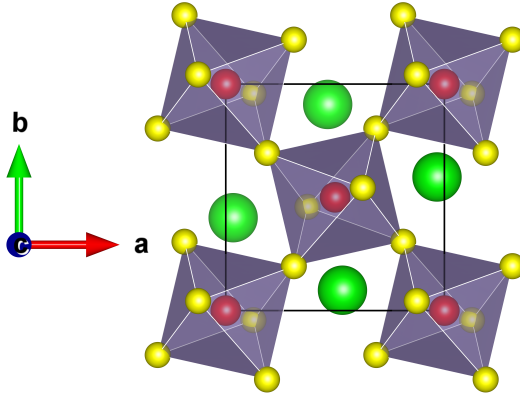


Figure 1. Crystal structure of the orthorhombic distorted phase for  $AGeX_3$  ( $A = \text{Ca, Sr, Ba}$ ;  $X = \text{S, Se}$ ) chalcogenide perovskites. Green, red, and yellow represent  $\text{Ca/Sr/Ba}$ ,  $\text{Ge}$ , and  $\text{S/Se}$  atoms, respectively.

##### 1. Crystal Structure:

In this study, we focus on the orthorhombic (space group  $Pnma$ ) phase of  $AGeX_3$  ( $A = \text{Ca, Sr, Ba}$ ;  $X = \text{S, Se}$ ) chalcogenide perovskites with a distorted perovskite structure. In this phase, the  $\text{Ge}$  atoms are sixfold coordinated with the X-site anions (S or Se), forming distorted and tilted  $[\text{GeX}_6]^{8-}$  corner sharing octahedras. Each unit cell of all the compounds, comprises 20 atoms: 4 A-site cations, 4 Ge atoms, and 12 X anions (see 1). The lattice parameters and bond lengths of the optimized compounds, calculated using the PBE xc functional, are tabulated in Table I.

The stability and structure of perovskite compounds ( $ABX_3$ ) can be qualitatively assessed using the Goldschmidt tolerance factor ( $t$ ) [47], a widely used geometric ratio defined as:

$$t = \frac{r_A + r_B}{\sqrt{2}(r_B + r_X)} \quad (1)$$

where  $r_A$ ,  $r_B$ , and  $r_X$  are the ionic radii of the A-site cation, B-site cation, and X-site anion, respectively. Ideal cubic perovskites have  $t=1$ , corresponding to a perfect B–X–B bond angle of  $180^\circ$  [48], while distorted perovskite structures generally fall within  $0.71 < t < 0.9$  [49]. This structural flexibility accommodates diverse elemental combinations at the A, B, and X-sites, enabling the exploration of unique properties [50–54]. The ionic radii values are typically sourced from Shannon’s effective ionic radii [55, 56]. Table S1 reveals that the  $t$  values for all compounds range from 0.89–0.98, validating the structural stability of these distorted chalcogenide perovskites.

Table I. Calculated lattice parameters, bond lengths and formation energies of  $AGeX_3$  ( $A = \text{Ca, Sr, Ba}$ ;  $X = \text{S, Se}$ ) chalcogenide perovskites.

Configurations	Lattice parameter			Bond length		$E_f$ (eV/atom)
	a (Å)	b (Å)	c (Å)	A–X (Å)	Ge–X (Å)	
CaGeS <sub>3</sub>	6.54	6.79	9.28	2.97	2.46	-0.832
CaGeSe <sub>3</sub>	6.99	7.23	9.64	3.12	2.62	-0.736
SrGeS <sub>3</sub>	6.60	7.03	9.49	3.09	2.41	-0.862
SrGeSe <sub>3</sub>	6.98	7.44	9.94	3.24	2.56	-0.791
BaGeS <sub>3</sub>	6.89	7.12	9.67	3.33	2.42	-0.877
BaGeSe <sub>3</sub>	7.21	7.50	10.18	3.40	2.58	-1.247

### 2. Thermodynamical Stability:

To examine the thermodynamic stability, we calculated the formation energy of our systems using the chemical formula:

$$E_f = \frac{E_{A_lGe_mX_n} - lE_A - mE_{Ge} - nE_X}{(l + m + n)} \quad (2)$$

where  $E_{A_lGe_mX_n}$  represents the optimized total energy of investigated compounds and  $E_A$ ,  $E_{Ge}$ , and  $E_X$  are the optimized energies of individual A-site, Ge, and X-site (S, Se) atoms in the crystal structure, respectively. The formation energy for all structures are determined using Eq. 2 and is presented in Table I. The results reveal that all the examined CPs possess negative formation energies, suggesting that these materials are thermodynamically stable under specific conditions.

### 3. Mechanical stability and elastic constants:

The elastic behavior of a material is widely recognized as a critical factor in determining its suitability for practical device applications. Therefore, we extended our analysis beyond crystallographic and thermodynamic stability to include mechanical stability by calculating the second-order elastic constants using the energy-strain approach [57]. All the compounds exhibit orthorhombic crystal symmetry, requiring nine independent elastic constants ( $C_{11}$ ,  $C_{22}$ ,  $C_{33}$ ,  $C_{44}$ ,  $C_{55}$ ,  $C_{66}$ ,  $C_{12}$ ,  $C_{13}$ , and  $C_{23}$ ) to describe their mechanical stability and elastic properties [9, 57]. The computed  $C_{ij}$  values for each CP are provided in Table S2. All values meet the Born stability criteria [57] (details in Section II of the Supplemental Material), confirming the exceptional mechanical stability of these orthorhombic phases. Additionally, these elastic coefficients are used to calculate the bulk modulus ( $B$ ), shear modulus ( $G$ ), Young's modulus ( $Y$ ), and Poisson's ratio ( $\nu$ ) for the materials [58, 59]. The brittle or ductile nature of the materials is assessed based on the critical thresholds for Pugh's ratio ( $B/G$ ) and Poisson's ratio ( $\nu$ ). Specifically, materials with  $\nu > 0.26$  and  $B/G > 1.75$  are classified as ductile, while those with lower values are considered brittle [60]. The results indicate that the investigated CPs exhibit greater resistance to volumetric deformation compared to shape deformation, as reflected by the higher  $B$  values relative to  $G$  (See Table S2). The lower  $G$  and  $Y$  values suggest a flexible nature of these materials. The values of Pugh's ratio ( $B/G$ ) and Poisson's ratio ( $\nu$ ) reveals, all the studied CPs are considered to be ductile.

### B. Electronic Properties:

Following the confirmation of structural stability, the electronic properties of  $AGeX_3$  ( $A = \text{Ca, Sr, Ba}$ ;  $X = \text{S, Se}$ ) CPs, including band structure, total and partial density of states (TDOS and PDOS), are analyzed to explore their potential for optoelectronic device applications. Initially, electronic structure calculations are performed using the GGA-PBE xc-functional [34], both with and without spin-orbit coupling (SOC). As expected for chalcogenide perovskites [19], SOC is found to have negligible impact on the bandgap, as can be seen from Table II. However, the PBE functional underestimates the bandgap due to self interaction error, prompted us to use the hybrid HSE06 [35] functional and many-body perturbation theory (MBPT) via the  $G_0W_0@PBE$  [36, 37] method for more accurate bandgap estimation. The  $G_0W_0@PBE$  calculated band structures are shown in Figure 2, revealing bandgap values ranging from 0.646 eV to 2.001 eV. For Ca- and Sr-based compounds, the valence band maxima (VBM) are located at the  $\Gamma$  (0, 0, 0) point of the Brillouin zone. In  $\text{CaGeS}_3$  and  $\text{CaGeSe}_3$ , the conduction band minima (CBM) are positioned between  $\Gamma$  and Z (0, 0, 0.5) and between  $\Gamma$  and X (0.5, 0, 0), respectively. In  $\text{SrGeS}_3$  and  $\text{SrGeSe}_3$ , the CBM is found at the T (0, 0.5, 0.5) point. For Ba-based compounds,  $\text{BaGeS}_3$  exhibits a VBM at U (0.5, 0, 0.5) and a CBM at T, while  $\text{BaGeSe}_3$  has both the VBM and CBM situated between T and Z, indicating an indirect bandgap. The HSE06 (0.516–1.177 eV) and  $G_0W_0@PBE$  (0.646–2.001 eV) bandgaps fall within the range suitable for optoelectronic applications. For example, the optimal bandgap range for solar cells is 0.9–1.6 eV [61], making some materials particularly favorable for photovoltaic applications, while others are better suited for alternative optoelectronic devices.

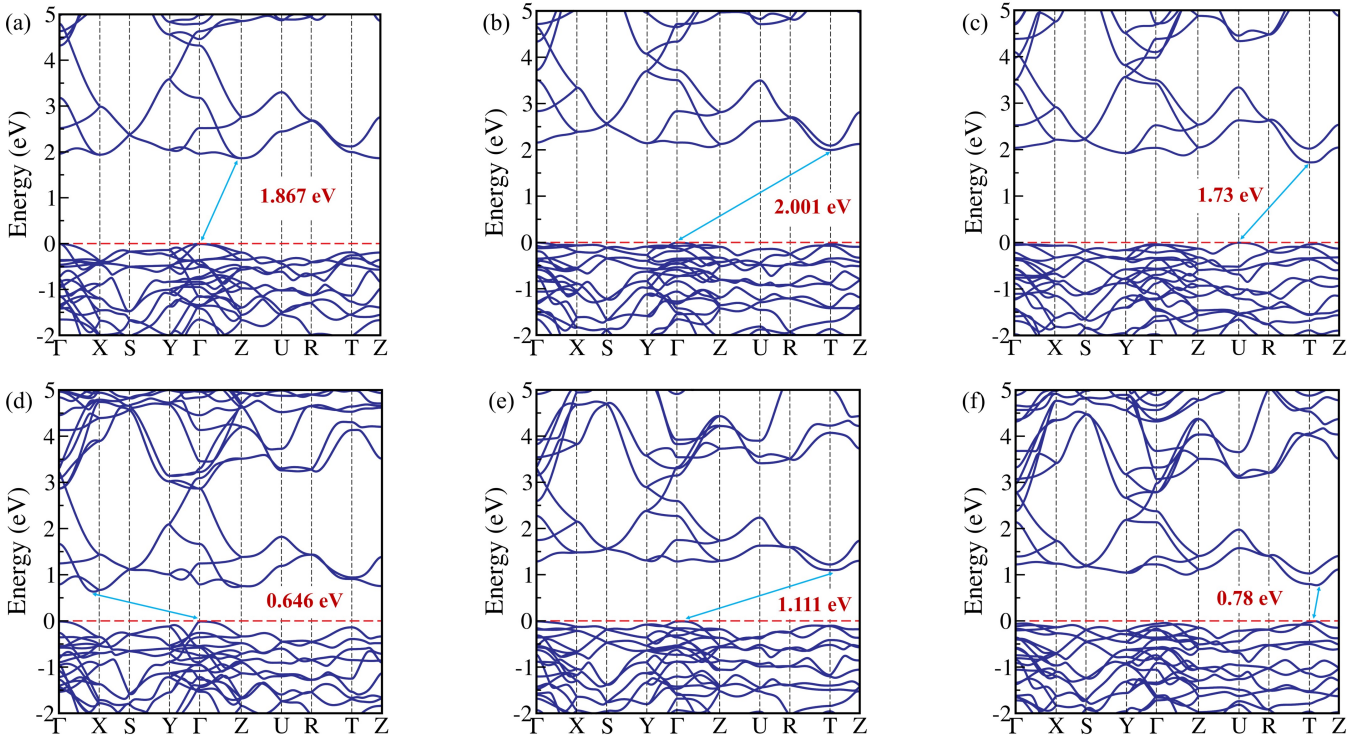


Figure 2. Electronic band structures of  $\text{AGeX}_3$  ( $A = \text{Ca}, \text{Sr}, \text{Ba}$ ;  $X = \text{S}, \text{Se}$ ) using the  $G_0W_0@PBE$  method. The Fermi level is set to be zero and marked by the dashed line.

The partial density of states (PDOS) and total density of states (TDOS) for all the studied compounds, calculated using the HSE06 xc functional, are depicted in Figure 3. In the  $\text{AGeS}_3$  ( $A = \text{Ca}, \text{Sr}, \text{Ba}$ ) CPs, VBM is predominantly derived from S-3*p* orbitals, while the CBM is primarily characterized by the hybridization of S-3*p* and Ge-4*s* orbitals. For the  $\text{AGeSe}_3$  counterparts, the VBM mainly originates from Se-4*p* orbitals, with a minor contribution from Ge-4*p* orbitals, whereas the CBM is dominated by the hybridization of Se-4*p* and Ge-4*s* orbitals. Notably, the hybridization between Se-4*p* and Ge-4*s* orbitals in  $\text{AGeSe}_3$  is more pronounced compared to the hybridization between S-3*p* and Ge-4*s* orbitals in  $\text{AGeS}_3$ . This stronger interaction in  $\text{AGeSe}_3$  contributes significantly to the reduction of the bandgap in selenium-based perovskites relative to their sulfur-based counterparts, highlighting a critical structural-electronic relationship in these materials.

To investigate the carrier transport properties of the studied perovskite materials, we calculated the effective masses of electrons ( $m_e^*$ ) and holes ( $m_h^*$ ) based on the band structure obtained from the  $G_0W_0@PBE$  approach. The effective masses were derived by computing the second-order derivatives of the energy dispersion relation ( $E - k$ ) near the band edges using the formula  $m^* = \hbar^2 [\partial^2 E(k)/\partial k^2]^{-1}$ , where  $\hbar$  is the reduced Planck's constant,  $E(k)$  represents the energy eigenvalue, and  $k$  is the wave vector. The effective masses are closely tied to the curvature of the conduction band minimum (CBM) and valence band maximum (VBM)-a greater curvature in these regions indicates lighter effective masses, which are essential for understanding the charge carrier dynamics in these materials. From Table III, it is evident that all compounds, except  $\text{BaGeS}_3$ , exhibit lower electron effective masses compared to hole effective masses, suggesting their suitability for n-type semiconductor applications. Since these compounds are indirect band gap materials, the effective masses were calculated at both the indirect and direct band edges. Interestingly,  $\text{BaGeS}_3$  shows a lower electron effective mass at its direct band edge, which may result from stronger band dispersion, enhancing electron mobility in direct band gap regions. The lower effective masses, particularly for electrons, indicate enhanced carrier mobility, which is beneficial for the efficient transport of charge carriers in these materials.

Table II. Computed bandgaps ( $E_g$ ) of  $\text{AGeX}_3$  ( $A = \text{Ca, Sr, Ba}$ ;  $X = \text{S, Se}$ ) chalcogenide perovskites using the PBE/PBE-SOC, HSE06 xc functionals, and  $G_0W_0@PBE$  method.

Configurations	$E_g$ (eV) (Indirect)			$E_g$ (eV) (Direct)		
	PBE/PBE-SOC	HSE06	$G_0W_0@PBE$	PBE/PBE-SOC	HSE06	$G_0W_0@PBE$
$\text{CaGeS}_3$	0.548/0.519	1.177	1.867	0.647/0.617	1.207	1.965
$\text{CaGeSe}_3$	-/-	0.517	0.646	-/-	0.567	0.802
$\text{SrGeS}_3$	0.671/0.643	1.326	2.001	0.696/0.684	1.345	2.026
$\text{SrGeSe}_3$	0.334/0.279	0.771	1.111	0.427/0.366	0.964	1.205
$\text{BaGeS}_3$	0.444/0.434	0.937	1.730	0.473/0.448	1.009	1.759
$\text{BaGeSe}_3$	0.173/0.121	0.516	0.780	0.174/0.144	0.520	0.781

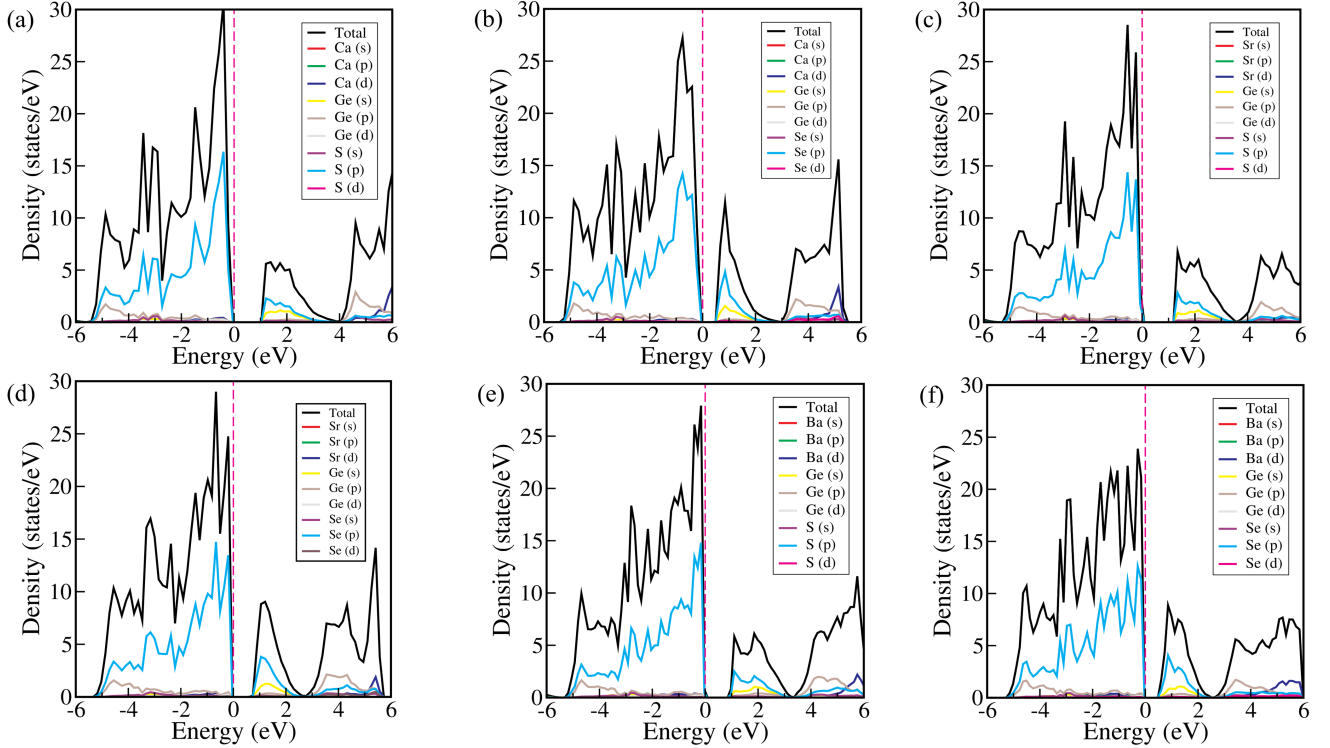


Figure 3. Calculated electronic total density of states (TDOS) and partial density of states (PDOS) of  $\text{AGeX}_3$  ( $A = \text{Ca, Sr, Ba}$ ;  $X = \text{S, Se}$ ) using the HSE06 xc functional. The Fermi level is set to be zero and marked by the dashed line.

### C. Optical Properties:

A thorough analysis of a material's optical properties, such as its dielectric function and absorption coefficient, is crucial for assessing its suitability for optoelectronic applications. While the HSE06 functional is effective in describing the electronic properties of the studied compounds, it is known to provide less accurate predictions for optical properties. To address this limitation and achieve higher accuracy, we employed many-body perturbation theory (MBPT)-based GW-BSE calculations, which explicitly account for electron-hole interactions. Single-shot GW calculations were performed on top of PBE to compute the fundamental bandgap, known to align closely with experimental techniques like photoelectron spectroscopy (PES) and inverse photoelectron spectroscopy (IPES) [36, 37]. Subsequently, the Bethe-Salpeter equation (BSE) was solved on the top of  $G_0W_0@PBE$  to determine the optical bandgap, which corresponds well with experimental optical absorption spectroscopy [44, 45].

Table III. Carrier's effective mass of  $AGeX_3$  ( $A = \text{Ca, Sr, Ba}$ ;  $X = \text{S, Se}$ ) chalcogenide perovskites. Here,  $m_e^*$  and  $m_h^*$  represents electron and hole effective mass (where  $m_0$  is the rest mass of the electron), respectively. The bold values provided in parentheses are the effective mass and reduced mass at indirect band edges.

Configurations	$m_e^*$ ( $m_0$ )	$m_h^*$ ( $m_0$ )	$\mu^*$ ( $m_0$ )
CaGeS <sub>3</sub>	0.401 ( <b>0.736</b> )	1.240 ( <b>2.230</b> )	0.303 ( <b>0.553</b> )
CaGeSe <sub>3</sub>	0.265 ( <b>0.330</b> )	1.638 ( <b>1.638</b> )	0.228 ( <b>0.275</b> )
SrGeS <sub>3</sub>	0.888 ( <b>1.039</b> )	1.187 ( <b>2.841</b> )	0.508 ( <b>0.761</b> )
SrGeSe <sub>3</sub>	0.553 ( <b>0.627</b> )	1.15 ( <b>1.284</b> )	0.373 ( <b>0.421</b> )
BaGeS <sub>3</sub>	0.864 ( <b>3.777</b> )	1.118 ( <b>2.738</b> )	0.487 ( <b>1.587</b> )
BaGeSe <sub>3</sub>	0.466 ( <b>0.317</b> )	0.322 ( <b>0.353</b> )	0.190 ( <b>0.284</b> )

The optical response was further analyzed by calculating the frequency-dependent dielectric function,  $\varepsilon(\omega) = [\text{Re}(\varepsilon)] + i [\text{Im}(\varepsilon)]$ , where  $\text{Re}(\varepsilon)$  and  $\text{Im}(\varepsilon)$  represent the real and imaginary components, respectively. Figure 4 illustrates the real and imaginary components of  $\varepsilon(\omega)$  evaluated using BSE@G<sub>0</sub>W<sub>0</sub>@ PBE. The real part of the dielectric function  $[\text{Re}(\varepsilon)]$  reflects the material's ability to polarize in response to an electromagnetic wave. The electronic dielectric constant ( $\varepsilon_\infty$ ), derived from this real part, quantifies how strongly electrons in the material respond to an electric field. A higher  $\varepsilon_\infty$  indicates stronger polarization, effectively screening the Coulomb interaction between electrons and holes, thereby reducing charge carrier recombination which is a key advantage for optoelectronic applications. Our results reveal that the studied compounds exhibit higher  $\varepsilon_\infty$  values compared to previously reported chalcogenide and halide perovskites [9, 62], highlighting their superior potential. Additionally,  $\varepsilon_\infty$  is observed to increase from sulfur-based to selenium-based CPs, suggesting reduced recombination rates and enhanced optoelectronic efficiency in the latter. The imaginary part of the dielectric function,  $\text{Im}(\varepsilon)$ , quantifies the extent of light energy absorbed by the material. Peaks in  $\text{Im}(\varepsilon)$  signify optical transitions, corresponding to the energy required to excite electrons from the valence band to the conduction band. The position of the first peak ( $E_o$ ) denotes the optical gap, representing the minimum photon energy necessary for electronic transitions. The  $E_o$  values of the studied compounds range from 0.513–1.420 eV, showing a redshift as the material composition changes from sulfur to selenium. This shift toward lower energies is in line with the reduction in quasiparticle bandgaps (see Table II) and suggests enhanced absorption in the infrared region. Such properties make these materials particularly suitable for applications in infrared optoelectronics and photovoltaics.

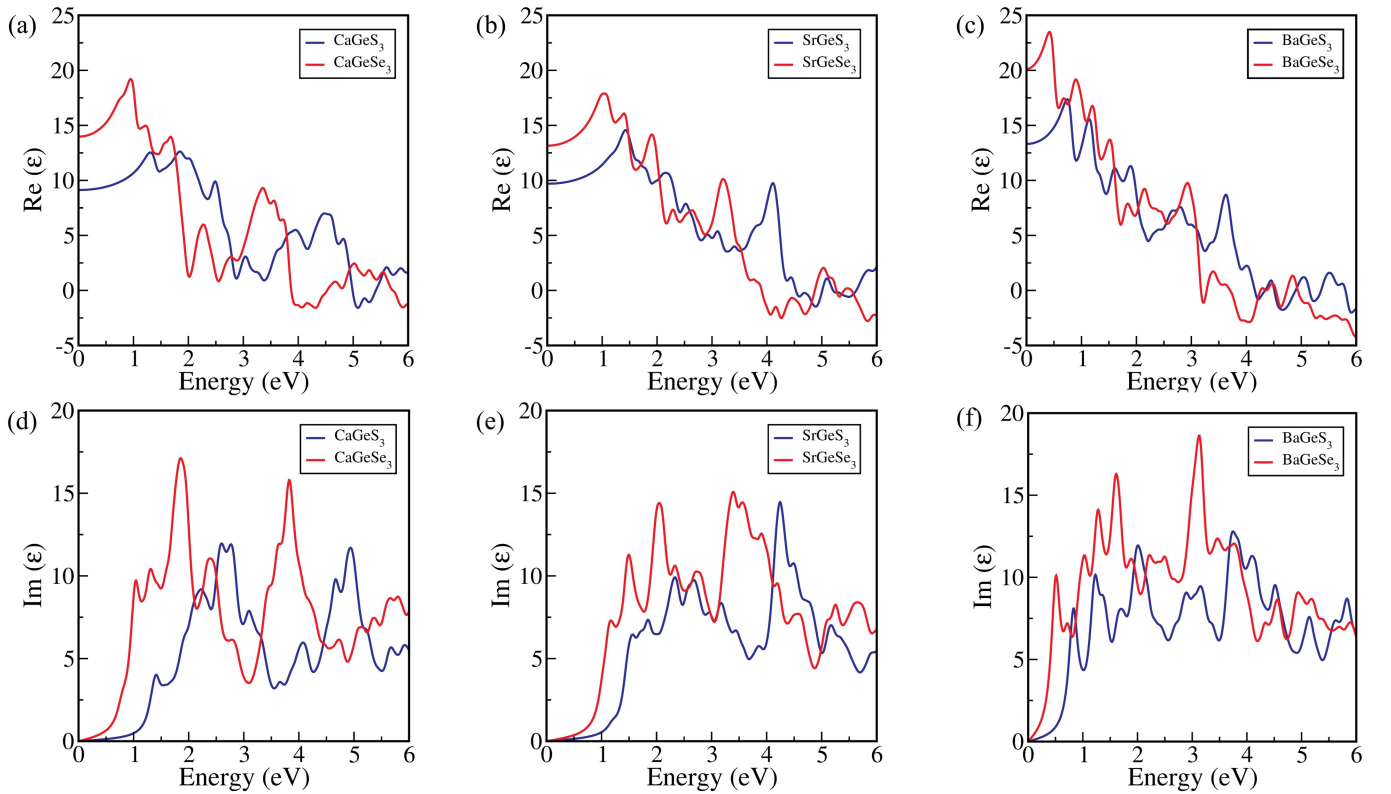


Figure 4. (a-c) Real [ $\text{Re}(\epsilon)$ ] and (d-f) imaginary [ $\text{Im}(\epsilon)$ ] parts of the dielectric function of chalcogenide perovskites obtained using the BSE@ $G_0W_0$ @PBE method.

#### D. Excitonic Properties:

Excitonic properties play a pivotal role in determining the charge separation efficiency of optoelectronic materials. Key parameters such as exciton binding energy ( $E_B$ ) and exciton lifetime ( $\tau_{exc}$ ) are critical for assessing their performance in practical applications. The exciton binding energy represents the energy required to dissociate a bound electron-hole pair into free carriers. In photovoltaic systems, a lower  $E_B$  enhances charge separation, contributing to improved photoelectric conversion efficiency.

In this study, the exciton binding energy ( $E_B$ ) is calculated using the Wannier-Mott model [9], which defines  $E_B$  as:

$$E_B = \left( \frac{\mu^*}{m_0 \epsilon_{\text{eff}}^2} \right) R_{\infty}, \quad (3)$$

where  $\mu^*$  is the reduced mass of charge carriers at direct band edges,  $m_0$  is the electron rest mass,  $\epsilon_{\text{eff}}$  represents the effective dielectric constant, and  $R_{\infty}$  is the Rydberg constant. The reduced mass ( $\mu^*$ ) is determined using the relation:

$$\frac{1}{\mu^*} = \frac{1}{m_e^*} + \frac{1}{m_h^*} \quad (4)$$

To compute  $E_B$ , the effective dielectric constant ( $\epsilon_{\text{eff}}$ ) must be evaluated. Previous studies suggest that  $E_B$  is influenced by lattice relaxation effects, particularly when  $E_B \ll \hbar\omega_{LO}$ , where  $\omega_{LO}$  is the longitudinal optical phonon frequency [63]. Under such conditions,  $\epsilon_{\text{eff}}$  is taken as an intermediate value between the static high-frequency dielectric constant ( $\epsilon_{\infty}$ ) and the low-frequency ionic dielectric constant ( $\epsilon_{\text{static}}$ ). However, for systems where  $E_B$  significantly exceeds  $\hbar\omega_{LO}$ , the electronic contribution dominates, and the ionic contribution becomes negligible. For chalcogenide perovskites, the electronic contribution is typically dominant [9, 19], allowing the use of  $\epsilon_{\infty}$  as an approximation for

$\varepsilon_{\text{eff}}$ . The calculated  $E_B$  values in this study, ranging from 6.38–73.63 meV (as depicted in Table IV), are significantly lower than those reported for other chalcogenide perovskites [10, 19], suggesting enhanced charge separation and, consequently, better optoelectronic performance.

Table IV. Calculated excitonic parameters and dielectric constants of  $\text{AGeX}_3$  ( $A = \text{Ca, Sr, Ba}$ ;  $X = \text{S, Se}$ ) chalcogenide perovskites. Here,  $\varepsilon_\infty$  is the electronic dielectric constant and  $E_B$  is the exciton binding energy (in unit meV).

Configurations	$\varepsilon_\infty$	$E_B$ (meV)	$r_{exc}$ (nm)	$ \phi_n(0) ^2$ ( $10^{26} m^{-3}$ )
$\text{CaGeS}_3$	9.12	49.58	1.59	0.79
$\text{CaGeSe}_3$	13.98	15.88	3.24	0.09
$\text{SrGeS}_3$	9.69	73.63	0.88	4.67
$\text{SrGeSe}_3$	13.16	29.31	1.87	0.49
$\text{BaGeS}_3$	13.32	37.36	1.45	1.04
$\text{BaGeSe}_3$	20.14	6.38	5.61	0.02

Furthermore, using the effective dielectric constant ( $\varepsilon_{\text{eff}}$ ), and the reduced mass of charge carriers ( $\mu^*$ ), several excitonic properties are calculated, including the excitonic radius ( $r_{exc}$ ), exciton lifetime ( $\tau_{exc}$ ), and the probability density of the electron-hole wavefunction at zero separation ( $|\phi_n(0)|^2$ ) is derived using the expression [19]:

$$|\phi_n(0)|^2 = \frac{1}{\pi(r_{exc})^3 n^3} \quad (5)$$

where  $r_{exc}$  represents the exciton radius, and  $n$  denotes the exciton energy level ( $n = 1$  provides the smallest exciton radius). The excitonic radius is calculated using the following formula [19]:

$$r_{exc} = \frac{m_0}{\mu^*} \varepsilon_{\text{eff}} n^2 r_{Ry} \quad (6)$$

where  $m_0$  is the rest mass of the electron, and  $r_{Ry}$  is Bohr radius (0.0529 nm). The parameters  $\varepsilon_{\text{eff}}$  and  $n$  are the same as defined earlier. The exciton lifetime ( $\tau_{exc}$ ) is inversely related to the probability of a wavefunction ( $|\phi_n(0)|^2$ ) for electron-hole pairs at zero charge separation (details in Section III of the Supplemental Material). In our study, all materials exhibit low  $|\phi_n(0)|^2$  (see Table IV) indicating prolonged exciton lifetimes. Notably, Se-containing compounds show even lower  $|\phi_n(0)|^2$  due to their larger exciton radius. This extended exciton lifetime reduces carrier recombination, enhancing conversion efficiency and making these materials highly suitable for photovoltaic applications.

### E. Polaronic Properties:

Electron-phonon coupling plays an essential role in shaping the physical and chemical properties of materials, profoundly influencing carrier dynamics and optoelectronic performance. In polar semiconductors, such as halide and chalcogenide perovskites, the interaction of charge carriers with longitudinal optical (LO) phonons significantly affects carrier mobility. This interaction, driven by the macroscopic electric field produced by LO phonons, dominates the scattering mechanism near room temperature [64]. To analyze this interaction for the studied materials, we employed the Fröhlich mesoscopic model [40], which quantifies the electron-phonon coupling through the dimensionless Fröhlich parameter ( $\alpha$ ) with the help of the following formula:

$$\alpha = \left( \frac{1}{\varepsilon_\infty} - \frac{1}{\varepsilon_{\text{static}}} \right) \sqrt{\frac{R_\infty}{ch\omega_{LO}}} \sqrt{\frac{m^*}{m_e}} \quad (7)$$

where  $\varepsilon_\infty$  and  $\varepsilon_{\text{static}}$  are the electronic and static dielectric constants, respectively, while  $h$  is Planck's constant,  $c$  is the speed of light, and  $R_\infty$  represents the Rydberg constant. A high  $\alpha$  value ( $\alpha > 10$ ) signifies strong coupling, while  $\alpha \ll 1$  indicates weak coupling [40]. The calculated  $\alpha$  values for  $\text{AGeX}_3$  CPs range from 0.78–5.39, indicating weak to intermediate electron (hole)-phonon coupling. Among the compounds,  $\text{BaGeSe}_3$  shows the weakest coupling, while  $\text{CaGeS}_3$  exhibits the strongest. Weak coupling is associated with lower electron effective mass and higher electronic dielectric constant, whereas stronger coupling correlates with the opposite trends.

Polaron formation can lead to a reduction in the energies of electron and hole quasiparticles (QPs). The corresponding polaron energy ( $E_p$ ) can be computed from  $\alpha$  using Eq. 8 as,

$$E_p = (-\alpha - 0.0123\alpha^2)\hbar\omega_{LO} \quad (8)$$

For CaGeS<sub>3</sub>, CaGeSe<sub>3</sub>, SrGeS<sub>3</sub>, SrGeSe<sub>3</sub>, BaGeS<sub>3</sub>, BaGeSe<sub>3</sub>, the QP energy is lowered by 0.108, 0.048, 0.089, 0.042, 0.109, 0.018 eV. On comparing these values with the  $E_B$  from Table IV, we conclude that the charge-separated polaronic state is more stable than the bound excitons [19].

The other polaron parameters, such as polaron mass ( $m_p$ ) and polaron mobility ( $\mu_p$ ) are critical for evaluating the material's optoelectronic potential. The polaron mass is calculated using the following relation [65]:

$$m_p = m^* \left( 1 + \frac{\alpha}{6} + \frac{\alpha^2}{40} + \dots \right) \quad (9)$$

where  $m^*$  is the effective mass of the charge carrier, and  $\alpha$  represents the electron-phonon coupling constant. A lower  $m_p$  indicates weaker carrier-lattice interactions, which is desirable for better optoelectronic performance. Next, the polaron mobility ( $\mu_p$ ) is determined with help of the Hellwarth polaron model [66]:

$$\mu_p = \frac{(3\sqrt{\pi}e)}{2\pi c\omega_{LO}m^*\alpha} \frac{\sinh(\beta/2)}{\beta^{5/2}} \frac{w^3}{v^3} \frac{1}{K} \quad (10)$$

where  $\beta = hc\omega_{LO}/k_B T$ ,  $e$  is the electronic charge,  $m^*$  represents the effective mass of the charge carriers,  $w$  and  $v$  are associated with temperature-dependent variational parameters (for details, see the Section V of the Supplemental Material).  $K$  is defined as follows:

$$K(a, b) = \int_0^\infty du [u^2 + a^2 - b \cos(vu)]^{-3/2} \cos(u) \quad (11)$$

Here,  $a^2$  and  $b$  are evaluated as:

$$a^2 = (\beta/2)^2 + \frac{(v^2 - w^2)}{w^2v} \beta \coth(\beta v/2) \quad (12)$$

$$b = \frac{v^2 - w^2}{w^2v} \frac{\beta}{\sinh(\beta v/2)} \quad (13)$$

In this work,  $\mu_p$  values range from 1.67 to 167.65 cm<sup>2</sup>V<sup>-1</sup>s<sup>-1</sup> (see Table V); encompassing low to very high polaron mobility. Notably, Se-containing compounds exhibit higher mobility due to weaker electron phonon coupling ( $\alpha$ ), with CaGeSe<sub>3</sub> and BaGeSe<sub>3</sub> compounds showing significantly higher  $\mu_p$  values compared to previous reports [9, 10, 19], reinforcing their better potential for optoelectronic applications.

Table V. Polaron parameters corresponding to electrons ( $e$ ) and holes ( $h$ ) in AGeX<sub>3</sub> (A = Ca, Sr, Ba; X = S, Se) chalcogenide perovskites. Here,  $\omega_{LO}$  represents the characteristic phonon angular frequency (in unit THz),  $\alpha$  represents Fröhlich interaction parameter,  $m_p$  represents effective mass of the polaron (in terms of  $m^*$ ),  $E_p$  represents polaron energy (in unit meV), and  $\mu_p$  represents the polaron mobility (in unit cm<sup>2</sup>V<sup>-1</sup>s<sup>-1</sup>), respectively.

Configurations	$\omega_{LO}$ (THz)	$\alpha$		$m_p/m^*$		$E_p$ (meV)		$\mu_p$ (cm <sup>2</sup> V <sup>-1</sup> s <sup>-1</sup> )	
		$e$	$h$	$e$	$h$	$e$	$h$	$e$	$h$
CaGeS <sub>3</sub>	3.01	3.10	5.39	1.76	2.62	38.62	68.97	13.13	1.68
CaGeSe <sub>3</sub>	3.29	1.05	2.33	1.20	1.52	14.89	33.55	102.66	8.43
SrGeS <sub>3</sub>	4.21	1.91	3.16	1.41	1.78	33.23	55.81	15.39	3.16
SrGeSe <sub>3</sub>	3.01	1.41	2.03	1.28	1.44	17.21	24.97	43.39	13.54
BaGeS <sub>3</sub>	3.67	3.76	3.23	1.98	1.80	59.01	50.37	1.67	2.90
BaGeSe <sub>3</sub>	2.56	0.78	0.82	1.15	1.15	8.66	9.11	167.65	142.45

#### IV. CONCLUSIONS:

To summarize, this study comprehensively explores the ground- and excited-state properties of Ge-based chalcogenide perovskites  $\text{AGeX}_3$  ( $\text{A} = \text{Ca, Sr, Ba}$ ;  $\text{X} = \text{S, Se}$ ), utilizing advanced DFT, DFPT, and MBPT (GW, BSE) methods. The materials demonstrate structural, thermodynamical, and mechanical stability, with band gaps calculated using the  $\text{G}_0\text{W}_0$ @PBE method, ranging from 0.646–2.001 eV. All the compounds having high charge carrier mobility, owing to small effective masses. The exciton binding energies (0.03–73.63 meV) are comparable to or lower than other chalcogenide perovskites, with a dominant electronic contribution to dielectric screening. Polaron mobility for electrons ( $1.67\text{--}167.65 \text{ cm}^2\text{V}^{-1}\text{s}^{-1}$ ) and holes ( $1.68\text{--}142.45 \text{ cm}^2\text{V}^{-1}\text{s}^{-1}$ ) further supports their excellent optoelectronic potential. These materials exhibit promising optical properties, making them ideal for a wide range of optoelectronic applications, including light-emitting diodes, photodetectors, and solar cells. Overall, the findings reveal the remarkable promise of Ge-based chalcogenide perovskites in advanced optoelectronic devices, offering a robust pathway toward efficient and sustainable next-generation technologies.

#### ACKNOWLEDGMENTS

A.C. would like to acknowledge the Shiv Nadar Institution of Eminence (SNIOE) for funding and support. S.A. would like to acknowledge the Council of Scientific and Industrial Research (CSIR), Government of India [Grant No. 09/1128(11453)/2021-EMR-I] for Senior Research Fellowship. The authors acknowledge the High Performance Computing Cluster (HPCC) ‘Magus’ at SNIOE for providing computational resources that have contributed to the research results reported within this paper.

- 
- [1] A. Kojima, K. Teshima, Y. Shirai, and T. Miyasaka, *J. Am. Chem. Soc.* **131**, 6050 (2009), pMID: 19366264, <https://doi.org/10.1021/ja809598r>.
- [2] National Renewable Energy Laboratory (NREL), (2021).
- [3] D. B. Straus, S. Guo, A. M. Abeykoon, and R. J. Cava, *Adv.Mater.* **32**, 2001069 (2020), <https://advanced.onlinelibrary.wiley.com/doi/pdf/10.1002/adma.202001069>.
- [4] A. Babayigit, A. Ethirajan, M. Muller, and B. Conings, *Nat. Mater.* **15**, 247 (2016).
- [5] D. Tiwari, O. S. Hutter, and G. Longo, *JPhys Energy* **3**, 034010 (2021).
- [6] W. Meng, B. Saparov, F. Hong, J. Wang, D. B. Mitzi, and Y. Yan, *Chem. Mater.* **28**, 821 (2016), <https://doi.org/10.1021/acs.chemmater.5b04213>.
- [7] K. V. Sopiha, C. Comparotto, J. A. Marquez, and J. J. S. Scragg, *Advanced Optical Materials* **10**, 2101704 (2022), <https://onlinelibrary.wiley.com/doi/pdf/10.1002/adom.202101704>.
- [8] K. Kuhar, A. Crovetto, M. Pandey, K. S. Thygesen, B. Seger, P. C. K. Vesborg, O. Hansen, I. Chorkendorff, and K. W. Jacobsen, *Energy Environ. Sci.* **10**, 2579 (2017).
- [9] S. Adhikari and P. Johari, *Phys. Rev. B* **109**, 174114 (2024).
- [10] P. Basera and S. Bhattacharya, *J. Phys. Chem. Lett.* **13**, 6439 (2022), pMID: 35816174, <https://doi.org/10.1021/acs.jpcclett.2c01337>.
- [11] S. Niu, H. Huyan, Y. Liu, M. Yeung, K. Ye, L. Blankemeier, T. Orvis, D. Sarkar, D. J. Singh, R. Kapadia, and J. Ravichandran, *Adv. Mater.* **29**, 1604733 (2017), <https://advanced.onlinelibrary.wiley.com/doi/pdf/10.1002/adma.201604733>.
- [12] Y.-Y. Sun, M. L. Agiorgousis, P. Zhang, and S. Zhang, *Nano Lett.* **15**, 581 (2015), pMID: 25548882, <https://doi.org/10.1021/nl504046x>.
- [13] D. Liu, H. Zeng, H. Peng, and R. Sa, *Phys. Chem. Chem. Phys.* **25**, 13755 (2023).
- [14] C.-S. Lee, K. M. Kleinke, and H. Kleinke, *Solid State Sci.* **7**, 1049 (2005).
- [15] N. A. Moroz, C. Bauer, L. Williams, A. Olvera, J. Casamento, A. A. Page, T. P. Bailey, A. Weiland, S. S. Stoyko, E. Kioupakis, C. Uher, J. A. Aitken, and P. F. P. Poudeu, *Inorg. Chem.* **57**, 7402 (2018), pMID: 29863367, <https://doi.org/10.1021/acs.inorgchem.8b01038>.
- [16] L. J. Tranchitella, B.-H. Chen, J. C. Fettinger, and B. W. Eichhorn, *J. Solid State Chem.* **130**, 20 (1997).
- [17] S. Perera, H. Hui, C. Zhao, H. Xue, F. Sun, C. Deng, N. Gross, C. Milleville, X. Xu, D. F. Watson, B. Weinstein, Y.-Y. Sun, S. Zhang, and H. Zeng, *Nano Energy* **22**, 129 (2016).
- [18] H. Shaili, M. Beraich, A. E. Hat, M. Ouafi, E. M. Salmani, R. Essajai, W. Battal, M. Rouchdi, M. Taibi, N. Hassanain, and A. Mzerd, *J. Phys. Chem. Lett.* **851**, 156790 (2021).
- [19] M. Kumar, A. Singh, D. Gill, and S. Bhattacharya, *J. Phys. Chem. Lett.* **12**, 5301 (2021), pMID: 34061540, <https://doi.org/10.1021/acs.jpcclett.1c01034>.
- [20] H. M. Ghaithan, S. M. H. Qaid, Z. A. Alahmed, M. Hezam, A. Lyras, M. Amer, and A. S. Aldwayyan, *J. Phys. Chem. C* **125**, 886 (2021), <https://doi.org/10.1021/acs.jpcc.0c07983>.

- [21] X. Chen, H. Lu, Y. Yang, and M. C. Beard, *J. Phys. Chem. Lett.* **9**, 2595 (2018), pMID: 29714488, <https://doi.org/10.1021/acs.jpcclett.8b00526>.
- [22] R. Guo and S. Wang, *J. Phys. Chem. C* **123**, 29 (2019), <https://doi.org/10.1021/acs.jpcc.8b08041>.
- [23] M.-G. Ju, J. Dai, L. Ma, and X. C. Zeng, *Adv. Energy Mater.* **7**, 1700216 (2017), <https://onlinelibrary.wiley.com/doi/pdf/10.1002/aenm.201700216>.
- [24] T. Tang and Y. Tang, *Inorg. Chem. Commun.* **171**, 113461 (2025).
- [25] H. Shaili, M. Beraich, A. E. Hat, M. Ouafi, E. M. Salmani, R. Essajai, W. Battal, M. Rouchdi, M. Taibi, N. Hassanain, and A. Mzerd, *J. Alloys Compd.* **851**, 156790 (2021).
- [26] S. An, H. Park, and M. Kim, *J. Mater. Chem. C* **11**, 2430 (2023).
- [27] K. Miyata and X.-Y. Zhu, *Nat. Mater.* **17**, 379 (2018).
- [28] S. Ponc e, M. Schlipf, and F. Giustino, *ACS Energy Lett.* **4**, 456 (2019), <https://doi.org/10.1021/acsenerylett.8b02346>.
- [29] P. Hohenberg and W. Kohn, *Phys. Rev.* **136**, B864 (1964).
- [30] W. Kohn and L. J. Sham, *Phys. Rev.* **140**, A1133 (1965).
- [31] M. Gajdoš, K. Hummer, G. Kresse, J. Furthm uller, and F. Bechstedt, *Phys. Rev. B* **73**, 045112 (2006).
- [32] H. Jiang, P. Rinke, and M. Scheffler, *Phys. Rev. B* **86**, 125115 (2012).
- [33] F. Fuchs, C. R odl, A. Schleife, and F. Bechstedt, *Phys. Rev. B* **78**, 085103 (2008).
- [34] J. P. Perdew, K. Burke, and M. Ernzerhof, *Phys. Rev. Lett.* **77**, 3865 (1996).
- [35] J. Heyd, G. E. Scuseria, and M. Ernzerhof, *J. Chem. Phys.* **118**, 8207 (2003), [https://pubs.aip.org/aip/jcp/article-pdf/118/18/8207/19093575/8207\\_1\\_online.pdf](https://pubs.aip.org/aip/jcp/article-pdf/118/18/8207/19093575/8207_1_online.pdf).
- [36] L. Hedin, *Phys. Rev.* **139**, A796 (1965).
- [37] M. S. Hybertsen and S. G. Louie, *Phys. Rev. Lett.* **55**, 1418 (1985).
- [38] R. Comin, G. Walters, E. S. Thibau, O. Voznyy, Z.-H. Lu, and E. H. Sargent, *J. Mater. Chem. C* **3**, 8839 (2015).
- [39] Q. Sun, H. Chen, and W.-J. Yin, *Chem. Mater.* **31**, 244 (2019), <https://doi.org/10.1021/acs.chemmater.8b04320>.
- [40] J. M. Frost, *Phys. Rev. B* **96**, 195202 (2017).
- [41] G. Kresse and J. Furthm uller, *Phys. Rev. B* **54**, 11169 (1996).
- [42] G. Kresse and J. Furthm uller, *Comput. Mater. Sci.* **6**, 15 (1996).
- [43] P. E. Bl ochl, *Phys. Rev. B* **50**, 17953 (1994).
- [44] S. Albrecht, L. Reining, R. Del Sole, and G. Onida, *Phys. Rev. Lett.* **80**, 4510 (1998).
- [45] M. R ohlfling and S. G. Louie, *Phys. Rev. Lett.* **81**, 2312 (1998).
- [46] V. Wang, N. Xu, J.-C. Liu, G. Tang, and W.-T. Geng, *Comput. Phys. Commun.* **267**, 108033 (2021).
- [47] W. Travis, E. N. K. Glover, H. Bronstein, D. O. Scanlon, and R. G. Palgrave, *Chem. Sci.* **7**, 4548 (2016).
- [48] A. Swarnkar, W. J. Mir, and A. Nag, *ACS Energy Lett.* **3**, 286 (2018), <https://doi.org/10.1021/acsenerylett.7b01197>.
- [49] Z. Li, M. Yang, J.-S. Park, S.-H. Wei, J. J. Berry, and K. Zhu, *Chem. Mater.* **28**, 284 (2016), <https://doi.org/10.1021/acs.chemmater.5b04107>.
- [50] H. J. Snaith, *Nat. Mater.* **17**, 372 (2018).
- [51] J. Hwang, R. R. Rao, L. Giordano, Y. Katayama, Y. Yu, and Y. Shao-Horn, *Science* **358**, 751 (2017),   2017 American Association for the Advancement of Science.
- [52] Y. Maeno, H. Hashimoto, K. Yoshida, S. Nishizaki, T. Fujita, J. G. Bednorz, and F. Lichtenberg, *Nature* **372**, 532 (1994).
- [53] R. Mahendiran, S. K. Tiwary, A. K. Raychaudhuri, T. V. Ramakrishnan, R. Mahesh, N. Rangavittal, and C. N. R. Rao, *Phys. Rev. B* **53**, 3348 (1996).
- [54] T. Choi, S. Lee, Y. J. Choi, V. Kiryukhin, and S.-W. Cheong, *Science* **324**, 63 (2009), <https://www.science.org/doi/pdf/10.1126/science.1168636>.
- [55] R. D. Shannon and C. T. Prewitt, *Acta Crystallogr., Sect. B: Struct. Crystallogr. Cryst. Chem.* **25**, 925 (1969).
- [56] R. D. Shannon, *Acta Crystallogr., Sect. A: Found. Crystallogr.* **32**, 751 (1976).
- [57] F. Mouhat and F. m. c.-X. Coudert, *Phys. Rev. B* **90**, 224104 (2014).
- [58] Z.-j. Wu, E.-j. Zhao, H.-p. Xiang, X.-f. Hao, X.-j. Liu, and J. Meng, *Phys. Rev. B* **76**, 054115 (2007).
- [59] R. Hill, *Proceedings of the Physical Society. Section A* **65**, 349 (1952).
- [60] S. Pugh, *The London, Edinburgh, and Dublin Philosophical. Mag. J. Sci.* **45**, 823 (1954), <https://doi.org/10.1080/14786440808520496>.
- [61] Q. Li, L. Zhou, Y. Ge, Y. Ren, J. Zhao, W. Wan, K. Zhang, and Y. Liu, arXiv preprint arXiv:1908.02187 (2019), arXiv:1908.02187 [physics.app-ph].
- [62] S. Adhikari and P. Johari, *Phys. Rev. Mater.* **7**, 075401 (2023).
- [63] C. Freysoldt, B. Grabowski, T. Hickel, J. Neugebauer, G. Kresse, A. Janotti, and C. G. Van de Walle, *Rev. Mod. Phys.* **86**, 253 (2014).
- [64] M. Jain, P. Bhumla, M. Kumar, and S. Bhattacharya, *J. Phys. Chem. C* **126**, 6753 (2022), <https://doi.org/10.1021/acs.jpcc.2c00102>.
- [65] R. P. Feynman, *Phys. Rev.* **97**, 660 (1955).
- [66] R. W. Hellwarth and I. Biaggio, *Phys. Rev. B* **60**, 299 (1999).